

performed, it can never be fully excluded that the anxiety- and goal-related firing described here may reflect more complex aspects and computations of the vCA1 network.

The mPFC and Amy are involved in anxiety behavior, receiving direct inputs from vCA1 (2, 4, 8). We demonstrated that anxiety-related activity is preferentially supported by vCA1 → mPFC projections, in agreement with described theta-frequency synchronization between the ventral hippocampus and mPFC during anxiety behavior (9). Nevertheless, the Amy could receive anxiety-related signals indirectly and processed them via the mPFC (10, 11). We hypothesize that vCA1 → Amy projections may rather contribute to contextual fear memories (12). Our results support a differential contribution of the dorsal and ventral hippocampus to spatial and anxiety behaviors (1, 13–15). Neural representations of space and anxiety coexist in vCA1 but are conveyed by distinct vCA1 projection types, which may receive segregated space and anxiety inputs from the Amy (16) or entorhinal cortex (17, 18). Alternatively, this segregation could be boosted by local parvalbumin-positive basket cells, which differentially inhibit CA1 projections targeting the Amy or mPFC (19). Additionally, projection type-specific plasticity could fine-tune the formation of place or anxiety neurons in vCA1 (20–23). Context-dependent fear renewal, conditioned place preference, or spatial working memory require spatial information to reach the Amy, Acb, or mPFC, respectively (24–26). We have demonstrated that place cells among vCA1 projection neurons indiscriminately target these areas and may support spatially driven cognitive processes. The wide-ranging presence of spatial information along the septotemporal axis of the hippocampus may coordinate the expression of interference and generalization, pertaining to mnemonic processes (27, 28).

We found two types of neuronal response among vCA1 projection neurons, with consistent trial-by-trial discharges in anticipation of reward outcomes, which were observed under numerous behavioral conditions, suggesting that this may be a universal phenomenon among subsets of vCA1 projection neurons. Goal-directed firing is conveyed to the Acb and mPFC by distinct vCA1 projections and may tune corticostriatal loops for goal-directed behavior (29, 30).

Our results indicate that higher cortical areas, such as the vCA1, communicate with other brain areas not by transmitting all of their computations equally but by routing the information according to content and recipient.

REFERENCES AND NOTES

- M. S. Fanselow, H. W. Dong, *Neuron* **65**, 7–19 (2010).
- L. A. Cenquizca, L. W. Swanson, *Brain Res. Brain Res. Rev.* **56**, 1–26 (2007).
- J. H. Jennings *et al.*, *Nature* **496**, 224–228 (2013).
- A. Adhikari, M. A. Topiwala, J. A. Gordon, *Neuron* **71**, 898–910 (2011).
- M. W. Jung, S. I. Wiener, B. L. McNaughton, *J. Neurosci.* **14**, 7347–7356 (1994).
- K. B. Kjelstrup *et al.*, *Science* **321**, 140–143 (2008).
- G. Girardeau, M. Zugaro, *Curr. Opin. Neurobiol.* **21**, 452–459 (2011).
- K. M. Tye *et al.*, *Nature* **471**, 358–362 (2011).
- A. Adhikari, M. A. Topiwala, J. A. Gordon, *Neuron* **65**, 257–269 (2010).
- E. Likhtik, J. M. Stujenske, M. A. Topiwala, A. Z. Harris, J. A. Gordon, *Nat. Neurosci.* **17**, 106–113 (2014).
- R. P. Vertes, *Synapse* **51**, 32–58 (2004).
- C. A. Orsini, J. H. Kim, E. Knapska, S. Maren, *J. Neurosci.* **31**, 17269–17277 (2011).
- S. Royer, A. Sirota, J. Patel, G. Buzsáki, *J. Neurosci.* **30**, 1777–1787 (2010).
- D. M. Bannerman *et al.*, *Nat. Rev. Neurosci.* **15**, 181–192 (2014).
- K. G. Kjelstrup *et al.*, *Proc. Natl. Acad. Sci. U.S.A.* **99**, 10825–10830 (2002).
- A. C. Felix-Ortiz *et al.*, *Neuron* **79**, 658–664 (2013).
- T. van Groen, P. Miettinen, I. Kadish, *Hippocampus* **13**, 133–149 (2003).
- S. J. Zhang *et al.*, *Science* **340**, 1232627 (2013).
- S. H. Lee *et al.*, *Neuron* **82**, 1129–1144 (2014).
- S. A. Hussaini, K. A. Kempadoo, S. J. Thualt, S. A. Siegelbaum, E. R. Kandel, *Neuron* **72**, 643–653 (2011).
- C. S. Kim, P. Y. Chang, D. Johnston, *Neuron* **75**, 503–516 (2012).
- A. Arszowski, Z. Borhegyi, T. Klausberger, *Front. Neuroanat.* **8**, 53 (2014).
- A. R. Graves *et al.*, *Neuron* **76**, 776–789 (2012).
- S. Maren, J. A. Hobin, *Learn. Mem.* **14**, 318–324 (2007).
- G. D. Carr, N. M. White, *Life Sci.* **33**, 2551–2557 (1983).
- M. W. Jones, M. A. Wilson, *PLOS Biol.* **3**, e402 (2005).
- R. W. Komorowski *et al.*, *J. Neurosci.* **33**, 8079–8087 (2013).
- A. T. Keinath *et al.*, *Hippocampus* **24**, 1533–1548 (2014).
- J. E. Lisman, A. A. Grace, *Neuron* **46**, 703–713 (2005).
- S. Ruediger, D. Spirig, F. Donato, P. Caroni, *Nat. Neurosci.* **15**, 1563–1571 (2012).

ACKNOWLEDGMENTS

We thank P. Schönerberger [Institute of Science and Technology (IST), Klosterneuburg, Austria] and S. Wolff (Harvard Medical School, Boston, USA) for helpful discussions on the optogenetic strategy; T. Asenov (IST) for three-dimensional printing of microdrives; R. Tomioka (Kumamoto University, Japan) for help in setting up the behavioral and electrophysiological experiments; E. Borok and R. Hauer for technical help with histology; all the members of the Klausberger lab for insightful discussions; and P. Somogyi, T. Viney, and M. Lagler for commenting on an earlier version of the manuscript. We thank Penn Vector Core from the University of Pennsylvania for the adeno-associated virus (AAV). The use of the AAV is disclosed by an materials transfer agreement between the University of Pennsylvania and the Medical University of Vienna. This work was supported in part by grant 242689 of the European Research Council and grant SCIC03 of the Vienna Science and Technology Fund. The authors declare that the research was conducted in the absence of any commercial or financial relationships that could be construed as a potential conflict of interest. Some of the original data are shown in the supplementary materials; all other data are available upon request from the corresponding authors.

SUPPLEMENTARY MATERIALS

www.sciencemag.org/content/348/6234/suppl/DC1
Materials and Methods

Figs. S1 to S14

Table S1

References (31–38)

18 November 2014; accepted 1 April 2015
10.1126/science.aaa3245

BIOMECHANICS

Mechanistic origins of bombardier beetle (Brachinini) explosion-induced defensive spray pulsation

Eric M. Arndt,¹ Wendy Moore,² Wah-Keat Lee,³ Christine Ortiz^{1*}

Bombardier beetles (Brachinini) use a rapid series of discrete explosions inside their pygidial gland reaction chambers to produce a hot, pulsed, quinone-based defensive spray. The mechanism of brachinines' spray pulsation was explored using anatomical studies and direct observation of explosions inside living beetles using synchrotron x-ray imaging. Quantification of the dynamics of vapor inside the reaction chamber indicates that spray pulsation is controlled by specialized, contiguous cuticular structures located at the junction between the reservoir (reactant) and reaction chambers. Kinematics models suggest passive mediation of spray pulsation by mechanical feedback from the explosion, causing displacement of these structures.

When threatened, bombardier beetles (Fig. 1A) expel a hot spray from their pygidial glands (1, 2). The spray contains *p*-benzoquinones (3), chemical irritants commonly employed by arthropods (4). However, bombardier beetles are unique in using

an internal explosive chemical reaction to simultaneously synthesize, heat, and propel their sprays (2, 3). The spray dynamics have been investigated by high-speed photography of the spray, spray impact force measurements, recordings of explosion sounds, and simulations (5–7). Species in the tribe Brachinini (brachinines) achieve spray temperatures of ~100°C (2), with ranges of several centimeters (1) and velocities of ~10 m/s via a “biological pulse jet” (5), where the spray consists of a rapid succession of pulses formed in discrete explosions. Pulse repetition rates of 368 to 735 Hz were measured from audio recordings for *Stenaptinus insignis* (5).

¹Department of Materials Science and Engineering, Massachusetts Institute of Technology (MIT), Cambridge, MA 02139-4307, USA. ²Department of Entomology, The University of Arizona, Tucson, AZ 85721-0036, USA.

³National Synchrotron Light Source II, Brookhaven National Laboratory, Upton, NY 11973-5000, USA.

*Corresponding author. E-mail: cortiz@mit.edu

It is well known that brachinines' ability to produce internal explosions is facilitated by the two-chambered construction of their pygidial glands (3) (Fig. 1, B to E). Each of the beetle's two pygidial glands comprises a reservoir chamber (RSC), reaction chamber (RXC), and exit channel (EC), which vents near the abdomen tip (Fig. 1B). The distal ends of the exit channels curve dorsally to form reflector plates (Fig. 1B, RP) used for spray aiming (8). An interchamber valve (Fig. 1, D and E, ICV) is contiguous with the walls of the reaction and reservoir chambers and separates the chambers' contents when closed (2). The pygidial glands are constructed of cuticle, a composite of chitin, proteins, and waxes (9) that protects the beetle from the toxic chemicals, high temperatures, and high pressures during explosions. The muscle-enveloped, flexible reservoir chamber (5) stores an aqueous reactant solution of ~25% hydrogen peroxide and ~10% *p*-hydroquinones (3), along with ~10% alkanes as a nonreactive

second liquid phase (10). Valve muscles (Fig. 1D, VM) span between the valve and the reservoir chamber to facilitate valve opening. During spray emission, reactant solution flows from the reservoir chamber into the reaction chamber, where it reacts with a solution of peroxidase and catalase enzymes (11) to form *p*-benzoquinones and explosively liberate oxygen gas, water vapor, and heat, propelling a hot, noxious spray out the exit channel.

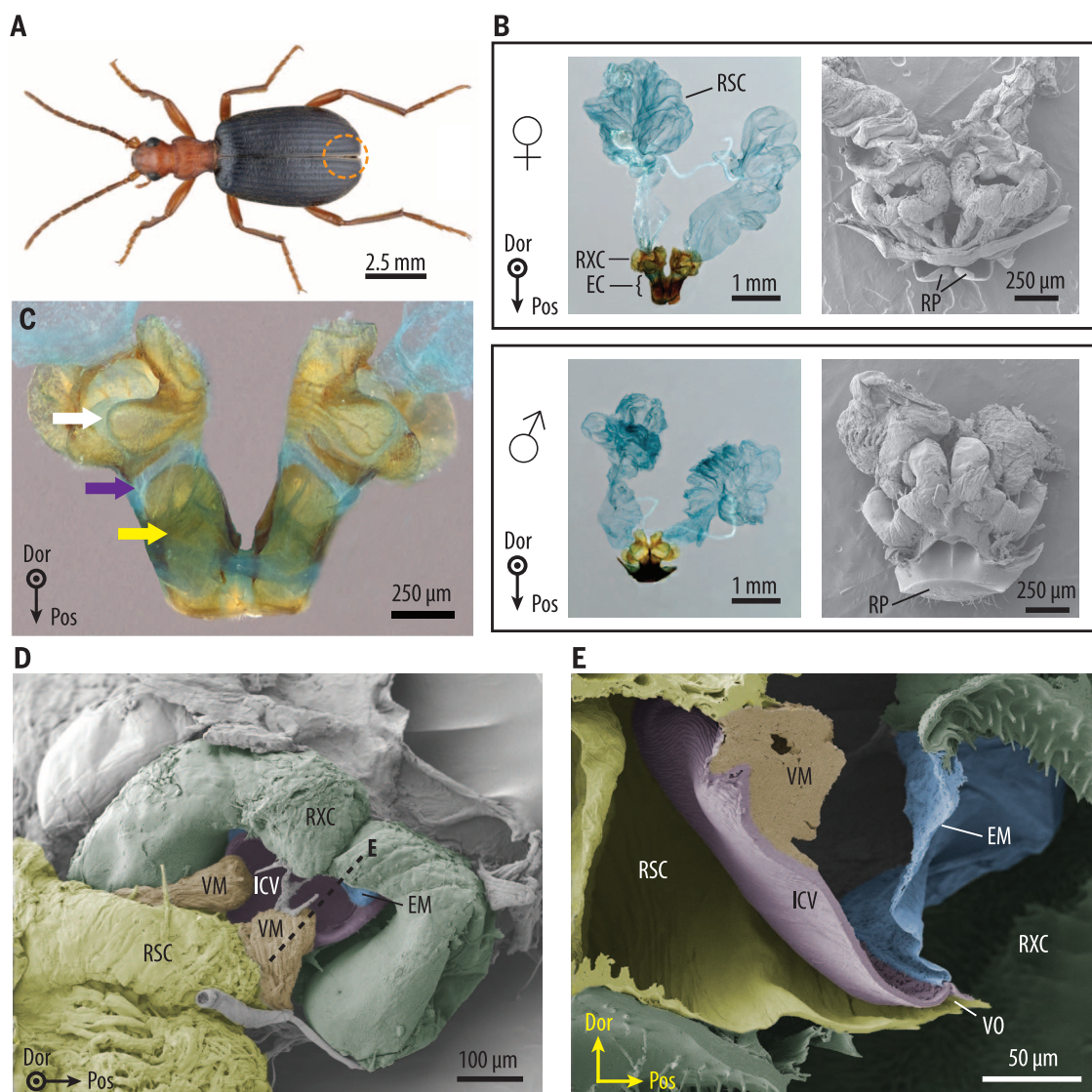
The mechanism of brachinines' spray pulsation has not been understood because previous studies, relying on external observations, have not probed internal dynamics. Here, we investigate this open question through optical and scanning electron microscopy to obtain new insights into the pygidial gland anatomy and synchrotron x-ray imaging (12–16) at up to 2000 frames per second (fps) to directly observe the internal dynamics of spray pulsation in live beetles (*Brachinus elongatulus*) (17). These experiments provide an

understanding of how explosions are initiated inside the pygidial glands and allow identification of the specific gland structures that mediate spray pulsation. An understanding of how brachinine pygidial glands produce (and survive) repetitive explosions could provide new design principles for technologies such as blast mitigation and propulsion.

Optical microscopy reveals that the reaction chamber exhibits dramatic spatial heterogeneity in cuticle sclerotization (Fig. 1C), corresponding to regions with different flexibility/rigidity (18) and, presumably, functional importance. The cuticle of most of the reaction chamber is tan or brown, implying heavy sclerotization and therefore high stiffness, which would serve to limit wall deflection and protect the beetle's internal tissues from the explosions. However, several regions are colorless (stained blue in Fig. 1, B and C, to increase contrast) and, hence, lightly sclerotized and compliant. These regions include the reaction

Fig. 1. *Brachinus elongatulus* pygidial gland morphology.

(A) Dorsal view. Dashed circle indicates location of pygidial glands. **(B)** Female (top) and male (bottom) pygidial glands: optical micrographs, chlorazol black staining (left) and SEM (right). Features are indicated: reservoir chamber (RSC), reaction chamber (RXC), exit channel (EC), and reflector plate (RP). **(C)** Female pygidial glands stained as in (B) showing rigid (highly sclerotized, brown/tan) and flexible (lightly sclerotized, stained blue) regions. Lightly sclerotized regions are identified: reaction chamber midline crease (white arrow); junction between reaction chamber and exit channel (purple arrow); exit channel dorsal membrane (yellow arrow). **(D)** False-color SEM showing valve muscles (VM), interchamber valve (ICV), and expansion membrane (EM). Other features labeled as in (B). Cross section shown in (E) is approximately normal to dashed line. **(E)** False-color SEM of cross section through interchamber region. The interchamber valve is observed in a closed conformation. Labels and colorization correspond to (D), with additional indication for the valve opening (VO).



chamber's dorsal midline crease and the junction between the reaction chamber and the exit channel (Fig. 1C). Similarly, the dorsal part of the exit channel is membranous and lightly sclerotized, whereas the ventral part is thick and heavily sclerotized (Fig. 1C) (6). Scanning electron microscopy (SEM) of the interchamber region in cross section (Fig. 1E) reveals that the cuticle that connects the valve to the dorsal part of the reaction chamber [hereafter called the expansion membrane (EM)] is very thin (~200 nm) and wrinkled, suggesting high flexibility.

Vapor formation during each explosion is clearly seen in the x-ray video as a bright region within the reaction chamber (Fig. 2A and movie S1). In the first pulse, vapor forms in the reaction chamber and propagates toward the exit channel. With each subsequent pulse, the vapor pocket initially expands slightly within the reaction chamber (implied by increased area) and then quickly contracts slightly as gas is ejected (Fig. 2A, first five pulses shown). Average pulsation rates calculated for 35 instances of gland activity from 18 sprays (median number of explosions, 13; range, 2 to 46) ranged from 341 to 976 Hz (median, 667 Hz; mean \pm SD, 698 ± 146 Hz) (fig. S1 and table S2). A linear fit to active time versus number of pulses predicts a pulsation rate of 650 Hz ($R^2 = 0.88$). These results are consistent with external experimental measurements of *S. insignis* (5) and approach the maximum rates reported for cyclic insect motions such as wing beats, measured as high as 1000 Hz for midges (19).

Each explosion corresponds to the injection of a reactant droplet into the reaction chamber, which can sometimes be seen as a dark circle in

relief against bright vapor (Fig. 2B and movie S2). Maximum diameters measured $208 \pm 7 \mu\text{m}$ (mean \pm SD) for four clearly visualized droplets. Assuming sphericity, the droplet volume is calculated to be $4.7 \pm 0.5 \text{ nL}$, and the mass is estimated as $5.5 \pm 0.6 \mu\text{g}$. Based on the theoretical heat of reaction of 0.8 J/mg (2), the estimated energy release for each explosion is $4 \times 10^{-3} \text{ J}$, and this energy liberates heat, boils water, and to a lesser extent provides the kinetic energy of the spray pulse. Estimating the spray pulse mass as equivalent to the droplet mass and taking 10 m/s for the spray exit velocity (5), the kinetic energy of a spray pulse is calculated to be $3 \times 10^{-7} \text{ J}$. Equating this energy to work done by pressure, the average overpressure in the reaction chamber is estimated as 20 kPa , producing wall tensile stresses of $\sim 1 \text{ MPa}$. For comparison, cuticle tensile strengths are typically tens to hundreds of megapascals (20). The time required to expel a pulse is estimated as 0.1 ms from the spray velocity and gland dimensions, consistent with the fact that explosions typically occur within single 2000-fps video frames (0.5 ms).

During each explosion, vapor is observed to fill a convex region between the reservoir and reaction chambers (Fig. 2A) that exceeds the dimensions of the reaction chamber indicated by microscopy (fig. S2), suggesting outward displacement of the expansion membrane driven by the explosion overpressure. Using the convex vapor shape as a proxy, the stretched expansion membrane can be modeled as a hemi-ellipsoid (fig. S2), and its maximum extension is found to be $\sim 280\%$ (see the supplementary text). For comparison, some insect cuticles exhibit recoverable extensions of

1000% (21). Based on the estimated overpressure and the estimated mass of the hemolymph displaced as the expansion membrane displaces into the body cavity, the expansion occurs with a maximum velocity of 6 m/s , attaining maximum displacement in 0.06 ms (supplementary text), consistent with the observation that expansion occurs within one video frame (0.5 ms). About one video frame after expansion is observed, the explosion reaction stops and vapor in the interchamber region contracts (e.g., Fig. 2A, frame 16), implying that the expansion membrane has returned to its unexpanded shape.

The exit channel of an active gland remains vapor-filled, and therefore open, throughout the entire pulse cycle (Fig. 2A and movies S1 to S3), possibly due to shape or mechanical characteristics (e.g., viscoelasticity) of its dorsal membrane, indicating that control of spray pulsation is accomplished by the reaction chamber inlet structures alone through opening and closing of the interchamber valve, as hypothesized previously (5). Typical cyclic mechanisms in insects (e.g., flapping flight and tymbal sound production) use multiple muscle sets that alternately contract or cuticular structures serving as springs (22), whereas the bombardier beetle possesses only valve-opening muscles and the valve is contiguous with flexible structures on all sides (i.e., reservoir chamber and expansion membrane). Hence, valve closure during each pulse cycle likely occurs passively due to mechanical feedback from the explosion, such as dynamic pressure from fluid (hemolymph) displaced by the expansion membrane, or impingement of the pressurized expansion membrane directly onto the valve, or a

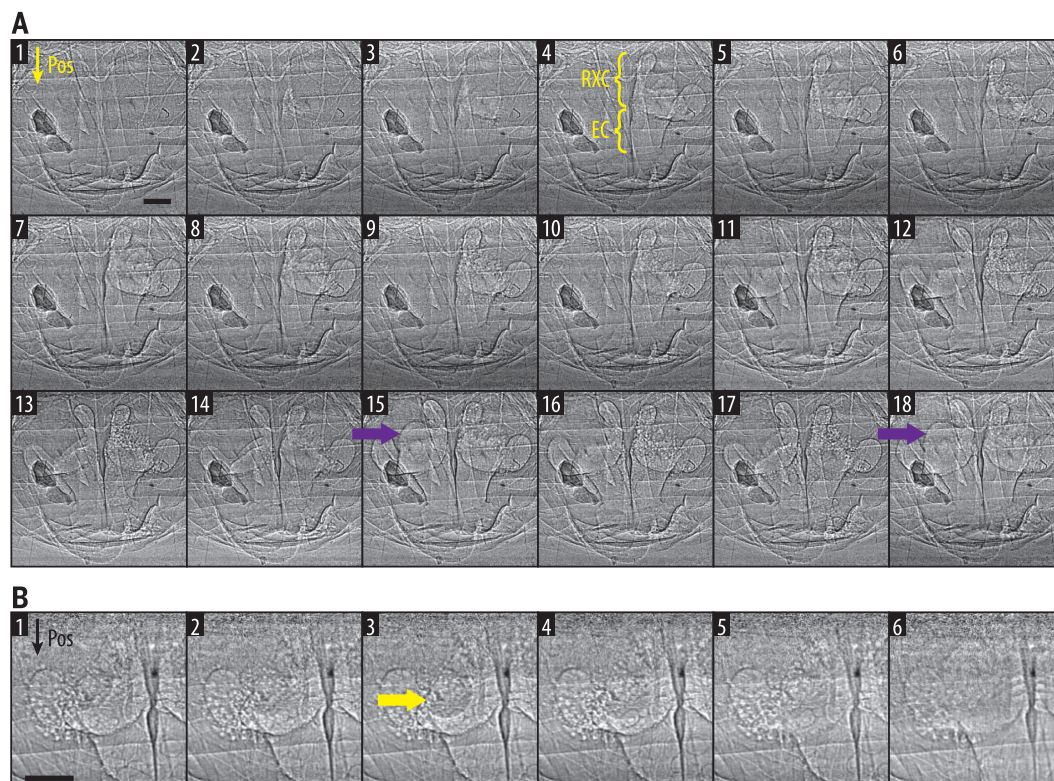


Fig. 2. Internal dynamics revealed by x-ray imaging.

(A) First five pulses of a spray; successive frames from 2000-fps video of a male beetle. Scale bar is $200 \mu\text{m}$. Location of right reaction chamber (RXC) and exit channel (EC) indicated in frame 4. Right and left exit channels are open starting in frames 4 and 11, respectively. Arrows indicate dramatic displacement of the expansion membrane. Dark objects at left are external debris. (B) Reactant droplet (arrow) entering reaction chamber and exploding; successive frames from 2000-fps video of a male beetle. Scale bar is $200 \mu\text{m}$.

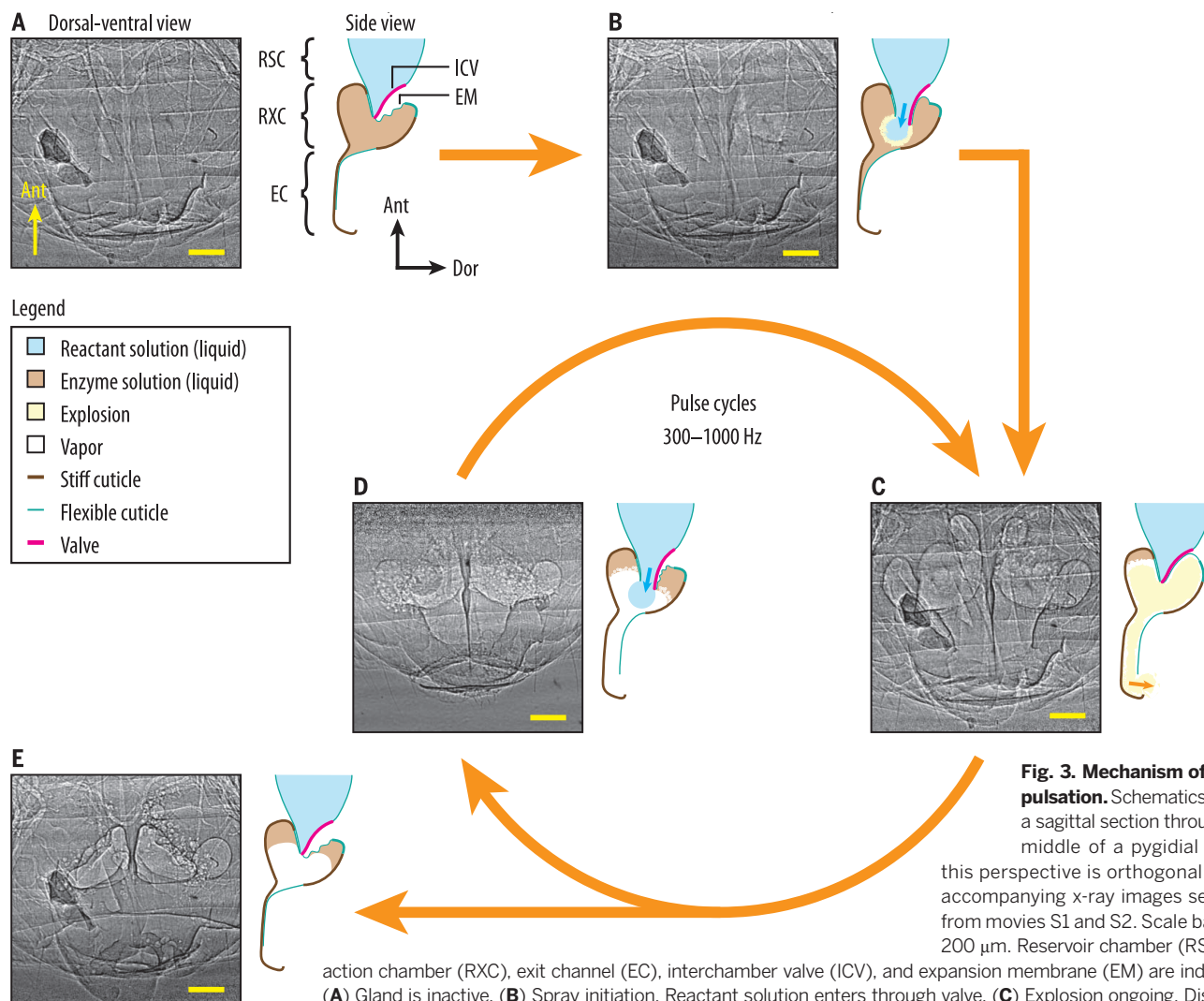


Fig. 3. Mechanism of spray pulsation. Schematics depict a sagittal section through the middle of a pygidial gland;

this perspective is orthogonal to the accompanying x-ray images selected from movies S1 and S2. Scale bars are 200 μm . Reservoir chamber (RSV), reaction chamber (RXC), exit channel (EC), interchamber valve (ICV), and expansion membrane (EM) are indicated.

(**A**) Gland is inactive. (**B**) Spray initiation. Reactant solution enters through valve. (**C**) Explosion ongoing. Displacement of expansion membrane closes the valve. A spray pulse is ejected. (**D**) Explosion ceases. Expansion membrane relaxes and valve reopens, permitting fresh reactant solution to enter. The process repeats C-D-C-D-C-D, and so on, with each “C-D” corresponding to one pulse cycle. (**E**) Spraying concluded. The exit channel closes and a vapor pocket remains in the reaction chamber.

combination of both. Simple kinematics models of these scenarios incorporating valve dimensions, the vapor expansion profile, and estimated overpressure discussed above predict forces that are sufficient to close the valve (supplementary online text).

Once the spray pulse is released and the overpressure in the reaction chamber drops, the load on the valve is removed, allowing it to reopen and permit a fresh reactant droplet to enter. It is not known whether the valve-opening muscles contract continually for the duration of spraying or once per pulse cycle, but both scenarios are compatible with passive valve closure and the capabilities of insect muscles (19).

The data presented suggest the following mechanism for spray pulsation (Fig. 3): The reservoir chamber musculature contracts for the duration of spraying to apply a continuous pressure to the reactant solution, and the valve muscles also contract, opening the interchamber valve and forcing a reactant droplet into the re-

action chamber (Fig. 3B). The droplet explodes upon contacting the reaction chamber enzymes (Fig. 3C), producing high-pressure vapor that propels a spray pulse out of the exit channel. Explosion overpressure displaces the expansion membrane and closes the interchamber valve, thereby interrupting the flow of reactants. After the explosion, the pressure in the reaction chamber decreases, the expansion membrane relaxes, the valve reopens, and a fresh reactant droplet enters, starting a new pulse cycle (Fig. 3D). Eventually, the reservoir and valve muscles relax, causing spraying to cease. The exit channel's dorsal membrane relaxes and collapses into its ventral trough, and some quantity of vapor generally remains in the reaction chamber as a pocket surrounded by numerous bubbles (Fig. 3E).

The pulsed spray mechanism of brachinine bombardier beetles is remarkably elegant and effective, protecting these beetles from nearly all predators (and incautious humans). The passive mediation of pulsation by mechanical feedback

from the explosion is advantageous because it provides automatic regulation of reactant use. Further, the evolutionary change from a continuous defensive spray (exhibited by close relatives of the brachinines) to a pulsed spray required only relatively minor changes to the reaction chamber inlet structures rather than the evolution of novel valve-closing muscles.

REFERENCES AND NOTES

1. T. Eisner, *J. Insect Physiol.* **2**, 215–220 (1958).
2. D. J. Aneshansley, T. Eisner, J. M. Widom, B. Widom, *Science* **165**, 61–63 (1969).
3. H. Schildknecht, K. Holoubek, K. H. Weis, H. Krämer, *Angew. Chem. Int. Ed. Engl.* **3**, 73–82 (1964).
4. M. S. Blum, *Chemical Defenses of Arthropods* (Academic Press, New York, 1981).
5. J. Dean, D. J. Aneshansley, H. E. Edgerton, T. Eisner, *Science* **248**, 1219–1221 (1990).
6. N. Beheshti, A. C. McIntosh, *Bioinspir. Biomim.* **2**, 57–64 (2007).
7. A. James, K. Morison, S. Todd, *J. R. Soc. Interface* **10**, 20120801 (2013).
8. T. Eisner, D. J. Aneshansley, *Proc. Natl. Acad. Sci. U.S.A.* **96**, 9705–9709 (1999).
9. S. O. Andersen, *Annu. Rev. Entomol.* **24**, 29–59 (1979).

10. T. Eisner *et al.*, *J. Insect Physiol.* **23**, 1383–1386 (1977).
11. H. Schildknecht, *Angew. Chem. Int. Ed. Engl.* **9**, 1–9 (1970).
12. M. W. Westneat *et al.*, *Science* **299**, 558–560 (2003).
13. J. J. Socha, M. W. Westneat, J. F. Harrison, J. S. Waters, W.-K. Lee, *BMC Biol.* **5**, 6 (2007).
14. J. J. Socha *et al.*, *J. Exp. Biol.* **211**, 3409–3420 (2008).
15. M. W. Westneat, J. J. Socha, W.-K. Lee, *Annu. Rev. Physiol.* **70**, 119–142 (2008).
16. W.-K. Lee, J. J. Socha, *BMC Physiol.* **9**, 2 (2009).
17. Materials and methods are available as supplementary materials on Science Online.
18. J. F. V. Vincent, J. E. Hillerton, *J. Insect Physiol.* **25**, 653–658 (1979).
19. O. Sotavalta, *Biol. Bull.* **104**, 439–444 (1953).
20. J. F. V. Vincent, U. G. K. Wegst, *Arthropod Struct. Dev.* **33**, 187–199 (2004).
21. J. F. V. Vincent, *Proc. R. Soc. London Ser. A* **188**, 189–201 (1975).
22. R. F. Chapman, *The Insects: Structure and Function* (Cambridge Univ. Press, Cambridge, ed. 5, 1998).

ACKNOWLEDGMENTS

Use of the Advanced Photon Source was supported by the U.S. Department of Energy, Office of Science, Office of Basic Energy Sciences, under contract DE-AC02-06CH11357. This work was supported in part by the U.S. Army Research Laboratory and the U.S. Army Research Office through the MIT Institute of Soldier Nanotechnologies under contract W911NF-13-D-0001 and in part by the National Science Foundation through the MIT Center for Materials Science and Engineering under contract DMR-08-19762. This research was funded in part by the U.S. Department of Defense, Office of the Director, Defense Research and Engineering, through the National Security Science and Engineering Faculty Fellowship awarded to C.O. under contract N00244-09-1-0064; in part by the National Science Foundation through funding awarded to W.M. under contract DEB-0908187; and in part by the U.S.

Department of Energy, Office of Science, Office of Basic Energy Sciences, under contract DE-SC0012704. Experiment data are available for download from DSpace@MIT (<https://dspace.mit.edu/>); please cite this collection using the handle hdl.handle.net/1721.1/96123.

SUPPLEMENTARY MATERIALS

www.sciencemag.org/content/348/6234/563/suppl/DC1
Materials and Methods
Supplementary Text
Figs. S1 to S3
Tables S1 and S2
Movies S1 to S3
References (23–32)

12 September 2014; accepted 16 March 2015
10.1126/science.1261166

EXTINCTIONS

Paleontological baselines for evaluating extinction risk in the modern oceans

Seth Finnegan,^{1,*} Sean C. Anderson,^{2,†} Paul G. Harnik,^{3,†} Carl Simpson,⁴ Derek P. Tittensor,^{5,6,7} Jarrett E. Byrnes,⁸ Zoe V. Finkel,⁹ David R. Lindberg,¹ Lee Hsiang Liow,¹⁰ Rowan Lockwood,¹¹ Heike K. Lotze,⁷ Craig R. McClain,¹² Jenny L. McGuire,¹³ Aaron O'Dea,¹⁴ John M. Pandolfi¹⁵

Marine taxa are threatened by anthropogenic impacts, but knowledge of their extinction vulnerabilities is limited. The fossil record provides rich information on past extinctions that can help predict biotic responses. We show that over 23 million years, taxonomic membership and geographic range size consistently explain a large proportion of extinction risk variation in six major taxonomic groups. We assess intrinsic risk—extinction risk predicted by paleontologically calibrated models—for modern genera in these groups. Mapping the geographic distribution of these genera identifies coastal biogeographic provinces where fauna with high intrinsic risk are strongly affected by human activity or climate change. Such regions are disproportionately in the tropics, raising the possibility that these ecosystems may be particularly vulnerable to future extinctions. Intrinsic risk provides a prehuman baseline for considering current threats to marine biodiversity.

Overfishing, habitat loss, pollution, climate change, and ocean acidification (1–4) pose intensifying threats to marine ecosystems, leading to concerns that a wave of marine extinctions may be imminent (5–10). In contrast to the terrestrial realm (11–13), little is known about the distribution of extinction vulnerability among marine taxa. Formal threat assessments have been conducted for a small and taxonomically biased subset of marine species (5, 9). These assessments are based primarily on the current distribution of species and their exposure to modern threats (14–17), but longer-term baseline data are a key component of any forecasting effort (18, 19). Knowledge of past extinction patterns is critical for predicting the factors that will determine future extinction vulnerability.

This knowledge can only come from the fossil record. Historical records are fragmentary for the marine realm, and few extinctions have been directly documented (5, 20). However, thick sequences of fossil-rich marine sediments are wide-

spread on all continents (21, 22) and chronicle the waxing, waning, and extinction of taxa within many ecologically important groups. The environmental drivers of current and future extinctions may differ from those of the past (5), but the considerable variation in rates and drivers of extinction over geological time scales (10⁵ to 10⁷ years) (5) provides an opportunity to determine whether there are predictors of extinction vulnerability that have remained consistent despite this variation. Such predictors can complement current risk assessments by identifying taxa that we expect to be especially vulnerable to extinction, given the macroevolutionary histories of taxa with similar characteristics. Here we construct models of extinction risk—defined as the probability of a fossil taxon being classified as extinct on the basis of its similarity to other fossil taxa that went extinct over the same interval of time—and use these models to evaluate the baseline extinction vulnerabilities of extant marine taxa. We use the term “intrinsic risk” to refer to pale-

ontologically calibrated estimates of baseline vulnerability for modern taxa.

We base our intrinsic risk evaluation on analyses of observed extinctions over the past 23 million years (Neogene-Pleistocene). We chose this interval to maximize faunal and geographic comparability between the modern and fossil data sets. The Neogene-Pleistocene fossil record is dominated by groups that are still extant and diverse, with continental configurations relatively similar to those of the present day. This interval also encompasses multiple extinction pulses and major changes in climatic and oceanographic conditions (e.g., contraction of the tropics, glacial-interglacial cycles, and associated changes in sea surface temperature and sea level) and is thus ideal for evaluating the consistency of extinction risk predictors. Using the Paleobiology Database (23), we analyzed Neogene-Pleistocene extinctions in six major marine taxonomic groups (bivalves, gastropods, echinoids, sharks, mammals, and scleractinian corals) for a total of 2897 fossil genera (table S1). We focused on these groups because they are generally well preserved in the fossil record (fig. S1) and are comparatively well sampled in modern coastal environments. Furthermore, these groups include several speciose

¹Department of Integrative Biology, University of California, Berkeley, CA 94720, USA. ²Department of Biological Sciences, Simon Fraser University, Burnaby, British Columbia V5A 1S6, Canada. ³Department of Earth and Environment, Franklin and Marshall College, Lancaster, PA 17604, USA. ⁴Department of Paleobiology, National Museum of Natural History, Washington, DC 20013, USA. ⁵United Nations Environment Programme World Conservation Monitoring Centre, Cambridge CB3 0DL, UK. ⁶Computational Science Laboratory, Microsoft Research, Cambridge CB1 2FB, UK. ⁷Department of Biology, Dalhousie University, Halifax, Nova Scotia B3H 4R2, Canada. ⁸Department of Biology, University of Massachusetts, Boston, MA 02125, USA. ⁹Environmental Science Program, Mount Allison University, Sackville, New Brunswick E4L 1A5, Canada. ¹⁰Center for Ecological and Evolutionary Synthesis, Department of Biosciences, University of Oslo, Blindern, N-0316 Oslo, Norway. ¹¹Department of Geology, College of William and Mary, Williamsburg, VA 23187, USA. ¹²National Evolutionary Synthesis Center, Durham, NC 27705, USA. ¹³School of Environmental and Forest Sciences, University of Washington, Seattle, WA 98195, USA. ¹⁴Smithsonian Tropical Research Institute, 0843-03092, Balboa, Republic of Panama. ¹⁵Australian Research Council Centre of Excellence for Coral Reef Studies, School of Biological Sciences, University of Queensland, St. Lucia, QLD 4072, Australia. *Corresponding author. E-mail: sethfin@berkeley.edu †These authors contributed equally to this work.

This copy is for your personal, non-commercial use only.

If you wish to distribute this article to others, you can order high-quality copies for your colleagues, clients, or customers by [clicking here](#).

Permission to republish or repurpose articles or portions of articles can be obtained by following the guidelines [here](#).

The following resources related to this article are available online at www.sciencemag.org (this information is current as of June 22, 2015):

Updated information and services, including high-resolution figures, can be found in the online version of this article at:

<http://www.sciencemag.org/content/348/6234/563.full.html>

Supporting Online Material can be found at:

<http://www.sciencemag.org/content/suppl/2015/04/29/348.6234.563.DC1.html>

This article **cites 25 articles**, 7 of which can be accessed free:

<http://www.sciencemag.org/content/348/6234/563.full.html#ref-list-1>

This article appears in the following **subject collections**:

Development

<http://www.sciencemag.org/cgi/collection/development>